Bicircular Light Floquet Engineering of Magnetic Symmetry and Topology and Its Application to the Dirac Semimetal Cd_3As_2

Thaís V. Trevisan,[1,2,*] Pablo Villar Arribi,[3,†] Olle Heinonen,[3] Robert-Jan Slager,[4,5] and Peter P. Orth[1,2,‡]
[1]*Ames Laboratory, Ames, Iowa 50011, USA*
[2]*Department of Physics and Astronomy, Iowa State University, Ames, Iowa 50011, USA*
[3]*Materials Science Division, Argonne National Laboratory, Lemont, Illinois 60439, USA*
[4]*TCM Group, Cavendish Laboratory, University of Cambridge, Cambridge CB3 0HE, United Kingdom*
[5]*Department of Physics, Harvard University, Cambridge, Massachusetts 02138, USA*

(Received 26 May 2021; revised 17 November 2021; accepted 10 January 2022; published 8 February 2022)

We show that bicircular light (BCL) is a versatile way to control magnetic symmetries and topology in materials. The electric field of BCL, which is a superposition of two circularly polarized light waves with frequencies that are integer multiples of each other, traces out a rose pattern in the polarization plane that can be chosen to break selective symmetries, including spatial inversion. Using a realistic low-energy model, we theoretically demonstrate that the three-dimensional Dirac semimetal Cd_3As_2 is a promising platform for BCL Floquet engineering. Without strain, BCL irradiation induces a transition to a noncentrosymmetric magnetic Weyl semimetal phase with tunable energy separation between the Weyl nodes. In the presence of strain, we predict the emergence of a magnetic topological crystalline insulator with exotic unpinned surface Dirac states that are protected by a combination of twofold rotation and time reversal $(2')$ and can be controlled by light.

DOI: 10.1103/PhysRevLett.128.066602

Introduction.—Recent years have seen a surge of interest in symmetry-protected topological phases with unique properties arising from a nontrivial topology of the bulk band structure. Examples are topological (crystalline) insulators [1–4] with dissipationless metallic surface states, magnetic axion insulators with large magnetoelectric couplings [5–7], and three-dimensional (3D) Dirac and Weyl semimetals (SMs) with exotic Fermi arc surface states [8]. Topological states also emerge in artificial systems such as cold atomic gases [9] and photonic waveguides [10]. The connection between symmetry and band topology is made explicit in classification schemes based on topological invariants like Chern and winding numbers [11], and in the more refined classification of crystalline materials using band compatibility relations [12–15], effectively generalizing the parity indicator of Fu and Kane [16]. A particularly rich set of symmetry-protected topological phases arises from magnetic symmetries, which combine time reversal (TR) with spatial symmetries, leading to a classification of phases in the 1651 magnetic space groups (MSGs) [17–19].

The relation between symmetry and topology not only facilitates the search for new realizations of symmetry-protected topological phases, but can also be employed to actively tune between different topological states by applying symmetry-breaking perturbations. Among them, periodic Floquet perturbations such as caused by irradiation with strong coherent light are particularly attractive since they allow for a *dynamic* manipulation on ultrafast time scales [20–25]. Floquet engineering of topological band structures has also been experimentally realized in artificial lattice systems [9,26–29] and photonic systems [10,30]. In real materials, light control of symmetry has been achieved via a direct Floquet dressing of electronic states using circularly polarized light (CL) [31,32], but also via exciting resonant lattice modes [33–37] and via photocurrent generation [38]. It was experimentally shown that TR breaking via CL irradiation can induce a quantum anomalous Hall state in topological insulator (TI) surface states [31] and in graphene [32,39].

Here, we show that Floquet engineering with bicircular light (BCL), which consists of a superposition of two CL waves with integer frequency ratio, offers an even greater tunability. The key idea is to use the polarization state of BCL to selectively break spatial symmetries, including inversion ($\mathcal{I}$), with direct consequences on band topology. This opens the possibility to realize noncentrosymmetric magnetic topological phases with unique, e.g., chiral and polar, properties. In two dimensions, the effect of BCL on graphene was recently discussed theoretically in Ref. [40]. We here propose to use BCL to tune 3D topological semimetallic and insulating parent phases, where the presence of a nodal point in the bulk or surface spectrum is protected by symmetries. Application of BCL can lift these symmetries and induce a desired topological phase transition by imposing a particular magnetic symmetry group from one of the subgroups of the crystal MSGs.

We emphasize that BCL Floquet engineering is a general approach that can be applied to a wide variety of systems including solid-state materials and artificial lattices. In the following, we consider a minimal model that describes general centrosymmetric 3D Dirac SMs and TIs. For concreteness and to make quantitative predictions, we consider model parameters that describes the 3D SM Cd_3As_2 [41] as an example. This material is a promising platform for BCL Floquet engineering, since high-mobility films are available [42] and the low-energy topological bands (arising from narrow As $4p$ states) are well separated in energy from other trivial bands by hundreds of meV [43]. This avoids heating of the topological states under a suitably chosen off-resonant Floquet drive in the mid- to near-infrared range.

Theory of BCL Floquet engineering.—BCL corresponds to the superposition of two CL waves with opposite chirality and frequencies that are an integer ratio η of each other. It is described by the vector potential

$$\mathbf{A}(t) = \mathcal{A}_0\sqrt{2}\mathrm{Re}[e^{-i(\eta\omega t-\alpha)}\boldsymbol{\varepsilon}_R + e^{-i\omega t}\boldsymbol{\varepsilon}_L], \tag{1}$$

where $\mathcal{A}_0$ is the amplitude and $\boldsymbol{\varepsilon}_{L/R}$ are left (L) and right (R) CL polarization basis vectors (for details, see Supplemental Material [44]). We assume uniform light illumination and neglect the photon momentum, as it is typically much smaller than system momenta. This vector potential, and the corresponding electric field, traces out a $(\eta+1)$-fold rose curve over a period $T = 2\pi/\omega$, as illustrated in Fig. 1(a). The spatial dependence of $\mathbf{A}(t)$ is crucial for breaking crystal symmetries that cannot be broken by CL, such as spatial inversion $\mathcal{I}$. Different magnetic symmetries can be broken by tuning the BCL frequency ratio η, which sets the rose pattern shape, the relative phase α, which promotes a rotation of the pattern, and the light incidence direction. We note that experimentally changing η and α is achieved by frequency selecting a particular higher-harmonic light mode with frequency $\eta\omega$ and by modifying the phase shift α between the fundamental and the higher-harmonic mode.

We consider BCL Floquet engineering in a generic four-band model describing centrosymmetric 3D Dirac SMs with two Dirac nodes near the Fermi level [43,45],

$$\hat{h}(\mathbf{k}) = M_{\mathbf{k}}\sigma_0\tau_z + \varepsilon_{\mathbf{k}}\sigma_0\tau_0 + P_{\mathbf{k}}\sigma_z\tau_x - Q_{\mathbf{k}}\sigma_0\tau_y. \tag{2}$$

Here, σ_i and τ_i are Pauli matrices in spin and orbital space, respectively. The momentum-dependent coefficients $M_{\mathbf{k}}$ and $\varepsilon_{\mathbf{k}}$ describe spin-independent hopping processes, and $P_{\mathbf{k}}$ and $Q_{\mathbf{k}}$ describe couplings between the orbital and the spin degrees of freedom. The underlying crystal symmetry enforces a certain form of the coefficients [44].

BCL couples to the system degrees of freedom via the standard Peierls substitution, $\hat{h}[\mathbf{k}+\mathbf{A}(t)]$. Choosing an off-resonant light frequency ω that is larger than the electronic

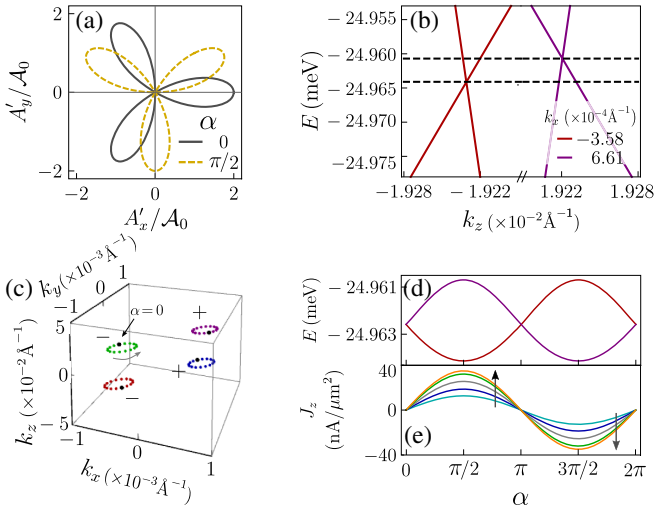

FIG. 1. BCL control of Weyl node locations in Cd_3As_2 and transport signature. (a) BCL vector potential $\mathbf{A}(t)$ for $\eta = 2$ and different α, leading to a rotation of the rose pattern. A'_x and A'_y refer to two orthogonal directions in the polarization plane. (b)–(d) Location of Weyl nodes in Cd_3As_2 as a function of α for BCL direction normal to (112) surface. (b) Cut of the bulk bands of the effective Hamiltonian in Eq. (3) for fixed $k_y = k_x$ and k_x as indicated. Here, we set $\omega = 5E_{\mathrm{Lif}} = 300$ meV, $\mathcal{A}_0 = 2.6\times10^{-2}$ Å^{-1}, and $\alpha = \pi/2$. A narrow energy window is shown to emphasize the energy separation of two of the Weyl nodes (see [44] for the full spectrum). (c) Trajectory of the Weyl nodes in momentum space as α evolves from 0 (black dots) to 2π. The Weyl nodes move counterclockwise, as indicated by the gray arrow. The signs indicate the chirality of each node. Other parameters are identical to the ones in (b). Note the different scales on k_x, k_y, and k_z axes. (d) Energy of Weyl nodes as a function of α. (e) Gyrotropic magnetic-effect-induced electric current as a response to a low-frequency oscillating magnetic field in the $\hat{z}$ direction as a function of α. We set the amplitude of the field to 3 T. Different colors refer to distinct values of $0.02 \le \mathcal{A}_0 \le 0.028$ Å^{-1} with increasing steps of 0.002 Å^{-1} in the direction of the arrows.

transition energies allows for the use of a high-frequency approximation [46–49]. This results in a time-independent effective Floquet-Bloch Hamiltonian

$$\hat{h}_{\mathrm{eff}}(\mathbf{k}) = \hat{h}_0(\mathbf{k}) + \hat{m}(\mathbf{k}), \tag{3}$$

$$\hat{m}(\mathbf{k}) = \frac{1}{\omega}\sum_{n=1}^{\infty}\frac{1}{n}[\hat{h}_n(\mathbf{k}), \hat{h}_{-n}(\mathbf{k})] + \mathcal{O}(\omega^{-2}). \tag{4}$$

Here, $\hat{h}_n(\mathbf{k}) = (1/T)\int_0^T dt e^{-in\omega t}\hat{h}[\mathbf{k}+\mathbf{A}(t)]$ is the nth Fourier component of the time-dependent Hamiltonian. We discuss higher-order contributions and corrections to the high-frequency regime in the Supplemental Material [44]. The two terms in Eq. (3) depend on the BCL polarization state and incidence direction and modify the bulk energy bands. Whereas $\hat{h}_0$, which is the time average of

TABLE I. Magnetic symmetries of Cd_3As_2 with and without light and lattice strain. Light incidence direction is perpendicular to the (112) surface and BCL parameter $\eta = 2$ (threefold rose pattern). The table shows the generators of the magnetic point group (MPG) preserved by the light and the resulting MSG for Cd_3As_2. Θ refers to TR symmetry and $\mathcal{I}$ to spatial inversion. The parameter α rotates the BCL rose pattern, which controls the MSG. The crystallographic axes [100], [010] and [001] of Cd_3As_2 are aligned with x, y and z, respectively [44].

Strain	Light type	α	MPG generators	MSG
0	No light	✗	C_{2z}, C_{4z}, C_{2y}, $\mathcal{I}$, Θ	$I4_1/acd1'$
	CL$\perp$(112)	✗	$\mathcal{I}$, $\Theta C_{2,[1\bar{1}0]}$	$C2'/c'$
	BCL$\perp$(112)	0, π	$\Theta M_{[1\bar{1}0]}$	Cc'
		$(\pi/2)$, $(3\pi/2)$	$\Theta C_{2,[1\bar{1}0]}$	$C2'$
		None of the above	1	$P1$
B_{1g}	No light	✗	C_{2z}, C_{2y}, $\mathcal{I}$, Θ	$Pcca1'$
	CL$\perp$(112)	✗	$\mathcal{I}$	$P\bar{1}$
B_{2g}	No light	✗	C_{2z}, $C_{2,[110]}$, $\mathcal{I}$, Θ	$Fddd1'$
	BCL$\perp$(112)	0, π	$\Theta M_{[1\bar{1}0]}$	Cc'
		$(\pi/2)$, $(3\pi/2)$	$\Theta C_{2,[1\bar{1}0]}$	$C2'$
		None of the above	1	$P1$

$\hat{h}[\mathbf{k} + \mathbf{A}(t)]$, merely shifts the position of the Dirac nodes, the light-induced mass term

$$\hat{m}(\mathbf{k}) = m_{1,\mathbf{k}}\sigma_z\tau_y + m_{2,\mathbf{k}}\sigma_0\tau_x + m_{3,\mathbf{k}}\sigma_z\tau_z \tag{5}$$

lifts the band degeneracy and drives topological transitions. Note that $\hat{m}(\mathbf{k})$ contains Pauli matrix products that are absent in the original model. The functions $m_{j,\mathbf{k}}$ involve combinations of $\hat{h}_n(\mathbf{k})$ (see [44] for their analytical form). Although CL and BCL generate the same set of terms in Eq. (5), the momentum dependence of $m_{j,\mathbf{k}}$ is different in the two cases, leading to a distinct symmetry breaking as shown in Table I.

BCL Floquet engineering of Cd_3As_2.—For concreteness, in the following we set $\eta = 2$ and focus on a parameter set in model (2) that describes the tetragonal 3D Dirac SM Cd_3As_2 [43,44,50,51]. This material exhibits two Dirac nodes located on the k_z axis, which are protected by fourfold rotation symmetry (C_{4z}). The characteristic low-energy scale describing the band inversion is given by the Lifshitz energy $E_{\mathrm{Lif}} = 60$ meV. Since trivial higher-energy bands are well separated in energy, the low-energy physics can be quantitatively described by a low-order expansion of the functions in Eq. (2) around $\mathbf{k} = 0$ [43,51].

Irradiation with BCL breaks both TR and $\mathcal{I}$ symmetries and thus results in a splitting of the two Dirac nodes into four Weyl nodes. Generically, they reside at different momenta and energies [see Figs. 1(b) and 1(c)], unless the presence of additional symmetries, which relate partner Weyl nodes with opposite chirality, forces these two to lie at the same energy. For example, for BCL incident normal to (112) and $\alpha = 0$ or π, one of the arms of the rose pattern aligns with the $[1\bar{1}0]$ axis [see x axis in Fig. 1(a)] and $m'_{[1\bar{1}0]}$ symmetry is preserved. Thus, two partner nodes connected by $m'_{[1\bar{1}0]}$ have the same energy. For all other values of α, the four nodes are separated both in energy and momentum. The energy separation between partner Weyl cones is quadratic in BCL amplitude $\mathcal{A}_0$ and scales as $1/\omega^2$. Thus, as α is varied between 0 and 2π, the Weyl nodes trace out closed loops in energy-momentum space [see Fig. 1(c)]. The size of the loop increases with the light amplitude $\mathcal{A}_0$, which opens the possibility of light-induced braiding of the Weyl nodes. Whereas in Cd_3As_2 we found that Weyl nodes of opposite chirality annihilate before braiding occurs, such a scenario may be possible in other models with larger Lifshitz energy or with Weyl nodes in different bulk gaps. Interestingly, braiding Weyl nodes in different gaps can change their frame charge, leading to the situation that nodes with equal net frame charge reside in a given gap [52–56]. As a consequence of the emergent obstruction to the annihilation of Weyl nodes, a new invariant emerges, known as the Euler class, which is yet to be fully explored.

The dynamical manipulation of the energy separation between the Weyl nodes has another interesting consequence if one applies an additional slowly oscillating magnetic field $\mathbf{B}(t)$. According to the gyrotropic magnetic effect [57,58], a noncentrosymmetric Weyl SM develops an electric current $\mathbf{J} \propto \mathbf{B}$ as a response, for which the amplitude is also proportional to the energy difference ΔE of partner Weyl nodes: $J = (e^2/3h^2)B\Delta E$. Importantly, ΔE can be controlled by the BCL amplitude $\mathcal{A}_0$ and the relative phase parameter α. We note that this effect requires the frequency of $\mathbf{B}$ to be smaller than the scale of interband

transitions, which is given by ΔE and lies in the 100 MHz range for the parameters of Fig. 1, and ultraclean samples, since the gyrotropic current is suppressed by disorder [44,57]. In the clean limit, we predict the gyrotropic current in BCL-driven Cd_3As_2 to lie within an experimentally accessible nA/μm^2 range for realistic electric field amplitudes $E_0 = \omega \mathcal{A}_0 \approx 10^7$ V/m and a magnetic field $B \approx 3$ T, which is modulated at less than megahertz frequencies [59]. Because of the linear dispersion around the Weyl nodes, the gyrotropic magnetic effect exhibits only a weak temperature dependence, and we predict it to be robust up to 10 K [44]. As shown in Fig. 1(e), the current J is modulated as a function of α and vanishes for $\alpha = 0, \pi$, where $\Delta E = 0$. To compute J, we have set the chemical potential equal to the energy of the pair of Weyl nodes in Fig. 1(b) at $\alpha = 0$. To reveal a unique signature of bulk Weyl nodes, we propose dynamically modulating $\alpha(t)$ on a frequency scale different from that of the magnetic field (e.g., in the gigahertz range) in order to change the gyrotropic current at the same frequency. Importantly, even in the unavoidable presence of interband transitions and heating in real materials, which is an inherent challenge in Floquet engineering, the coherent modulation of the gyromagnetic current can still be detected in a lock-in type experiment, since incoherent effects and heating are independent of α.

Finally, light irradiation also impacts the shape, curvature, and position of the Fermi arc surface states in Cd_3As_2, which allows one to manipulate surface transport properties [60]. Figure 2 shows Fermi arc surface states on the experimentally accessible (112) surface [42] at fixed energy, both without light and in the presence of CL or BCL. The geometry of the Fermi arcs, which connect projections of the nodal points onto the (112) surface, is different for CL and BCL [44].

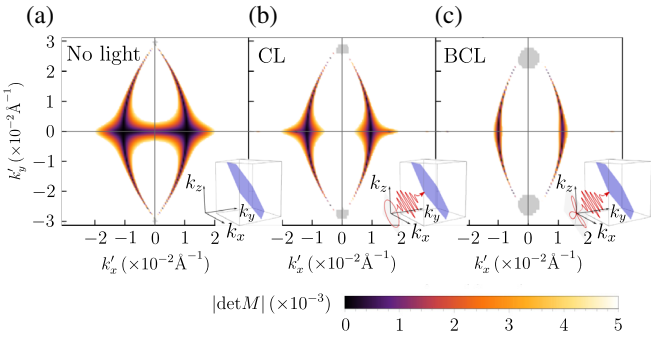

FIG. 2. Effect of CL and BCL on Fermi arc surface states at energy $E = -E_{\text{Lif}}/2 = -30$ meV, the location of Dirac nodes in the absence of light, on the (112) surface of Cd_3As_2 (shown in blue in the insets). k_x' and k_y' are components of the surface momentum along directions $[1\bar{1}0]$ and $[11\bar{1}]$, respectively. The gray regions correspond to the projection of bulk states onto the surface. Different panels show surface states: (a) in the absence of light, (b) for CL with light direction normal to (112), (c) for BCL with light direction normal to (112). (b),(c) We set $\omega = 5E_{\text{Lif}} = 300$ meV, $\mathcal{A}_0 = 2 \times 10^{-2}$ Å^{-1}, and $\alpha = 0$. The condition $\det M = 0$ reflects our choice of boundary condition and can be interpreted as finite overlap to bulk states [44]. Note that the results in (c) depend only weakly on the value of α.

Floquet engineering of strained Cd_3As_2.—Under the influence of lattice strain that breaks C_{4z} symmetry, Cd_3As_2 becomes a strong TI with gapless Dirac surface states on every crystal surface. In the following, we consider experimentally realistic types of strain: First, B_{1g}-symmetric strain that breaks C_{4z} and the twofold rotations along the diagonals, $C_{2,[110]}$ and $C_{2,[1\bar{1}0]}$ [42,51]. We also consider B_{2g}-symmetric strain that breaks C_{4z} and the twofold rotations along the crystallographic axes, C_{2x} and C_{2y}. Within the generic four-band model in Eq. (2), B_{1g} and B_{2g} strains correspond to terms of the form $B_{\mathbf{k}}\sigma_x\tau_x$ and $B_{\mathbf{k}}\sigma_y\tau_x$, respectively, where $B_{\mathbf{k}} \propto k_z$. Additional terms that renormalize the parameters in Eq. (2) are allowed by symmetry, but vanish along k_z and thus do not contribute to the size of the bulk gap. Under irradiation these strain terms lead to additional light-induced mass terms beyond those listed in Eq. (5) that also contribute to magnetic symmetry breaking (see [44]). As we show next, this opens up an interesting possibility of inducing sought-after topological states protected by magnetic symmetries. Specifically, we predict a CL-induced axion insulator state [61] and a BCL-induced magnetic topological crystalline insulator protected by $2'$ symmetry [62,63].

Table I shows that the combination of B_{1g} strain and CL irradiation along the (112) normal removes all symmetries except $\mathcal{I}$. Since the bulk gap remains open for not too large light intensities, we can conclude that CL induces a topological transition to an axion insulator state with quantized magnetoelectric coupling and half-quantized anomalous surface Hall conductivity [5]. As $\mathcal{I}$ is naturally broken at the surface, the surface states acquire a gap as shown in Fig. 3 for the particular case of the (001) surface.

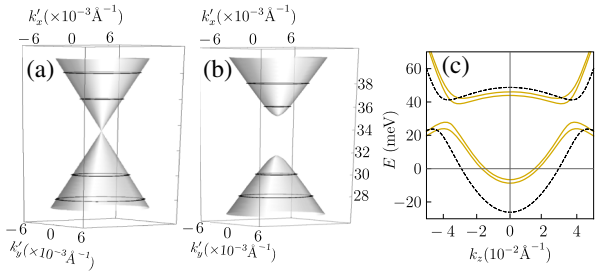

FIG. 3. CL-induced topological transition from topological to axion insulator gaps out the surface states in the (001) surface of Cd_3As_2 under B_{1g} strain. (a) In the absence of light and (b) in the presence of CL with $\omega = 5E_{\text{Lif}} = 400$ meV and $\mathcal{A}_0 = 2.4 \times 10^{-2}$ Å^{-1}, incident normal to (112), as in the inset of Fig. 2(b). Here, k_x' (k_y') points along the [100] ([010]) direction. (c) Cut of the bulk bands of strained Cd_3As_2 for fixed $k_x = k_y = 0$ in absence (dashed) and presence (solid) of CL light with the same parameters as in (b).

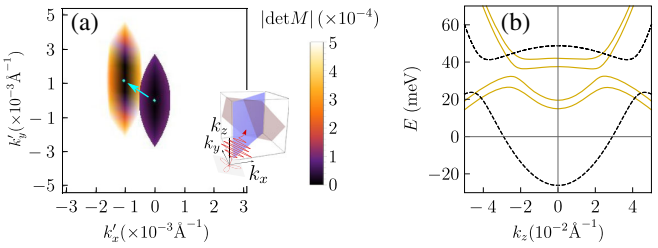

FIG. 4. BCL control of Dirac node position in light-induced $2'$ axion insulator state. (a) The evolution of gapless surface states in the $(1\bar{1}0)$ surface of Cd_3As_2 (blue plane in the inset) in presence of B_{2g} strain when turning on BCL. Here, k_x' (k_y') are components along the [110] ([001]) directions. The ellipse centered around $k_x' = k_y' = 0$ is a fixed-energy cut of the surface state at 37 meV close to the node in the absence of light. BCL irradiation along direction normal to (112) (red plane in the inset) induces a $2'$ magnetic topological crystalline insulator with unpinned Dirac surface states. The surface state moves in the direction indicated by the arrow when BCL is turned on, while the energy of the Dirac node changes only slightly to 36 meV. Color shows $\det M$, which has the same meaning as in Fig. 2. (b) Bulk energy bands of strained Cd_3As_2 for fixed $k_x = k_y = 0$ without light (dashed) and with BCL (solid). In both panels, we set $\omega = 150$ meV, $\mathcal{A}_0 = 2.6 \times 10^{-2}$ Å^{-1}, $\alpha = \pi/2$.

An even more intriguing situation arises in the presence of B_{2g} strain and BCL irradiation along (112) normal. Choosing α as either $(\pi/2)$ or $(3\pi/2)$ removes all symmetries except the combination of a twofold rotation around $[1\bar{1}0]$ and time reversal: $\Theta C_{2,[1\bar{1}0]} \equiv 2'_{[1\bar{1}0]}$. Since a $2'$ operation reverses an odd number of spacetime coordinates (like TR and $\mathcal{I}$), the magnetoelectric coupling is still quantized [64]. Again, for light intensities that leave the bulk gap open, continuity ensures that BCL induces a topologically nontrivial axion insulator state. Here, however, not all surfaces are gapped. Instead, $(1\bar{1}0)$ surfaces (whose surface normal is parallel to the $2'$ axis) host exotic gapless Dirac states for which the nodal position is unpinned from the surface TR invariant momenta. As shown in Fig. 4, the position of the nodal point is controlled by light parameters such as frequency and intensity [44]. All other surfaces are gapped and exhibit a half-quantized anomalous surface Hall conductivity.

Conclusion.—To conclude, we show that Floquet engineering using BCL offers wide tunability of the magnetic symmetries of a system beyond the capabilities of linear or circularly polarized light. This arises from the fact that the electric field of BCL follows a rose pattern that can be tailored to break desired spatial inversion and other symmetries, in addition to time reversal, leading to a noncentrosymmetric effective Floquet-Bloch Hamiltonian. This general approach of BCL tuning of symmetries is applicable to a wide variety of materials and artificial lattice system and can have immediate impact on their band topology. As a concrete example, we predict effects of Floquet engineering in the Dirac SM Cd_3As_2, which is a suitable material platform that undergoes various light-induced topological phase transitions. In the absence of strain, BCL leads to a noncentrosymmetric magnetic Weyl SM phase with bulk nodes separated in both energy and momentum. We demonstrate that the position of the nodes can be controlled via light parameters, opening up the possibility of braiding. In the presence of an additional slowly varying magnetic field, BCL leads to a tunable dissipationless current due to the gyrotropic magnetic effect, which is a unique signature of Weyl physics. Finally, combining lattice strain and BCL irradiation realizes a sought-after magnetic axion insulator phase with exotic unpinned surface states protected by $2'$ symmetry.

We thank A. Burkov, R. McDonald, V. L. Quito, S. Stemmer, and D. Yarotski for useful discussions. This research was supported by the Center for Advancement of Topological Semimetals, an Energy Frontier Research Center funded by the U.S. Department of Energy Office of Science, Office of Basic Energy Sciences, through the Ames Laboratory under Award No. DE-AC02-07CH11358. R.-J. S. acknowledges funding from the Marie Skłodowska-Curie program under EC Grant No. 842901 and the Winton program, as well as Trinity College at the University of Cambridge.

*thais@iastate.edu
†Present address: International School for Advanced Studies (SISSA), Via Bonomea 265, I-34136 Trieste, Italy.
‡porth@iastate.edu

[1] M. Z. Hasan and C. L. Kane, Rev. Mod. Phys. **82**, 3045 (2010).
[2] X.-L. Qi and S.-C. Zhang, Rev. Mod. Phys. **83**, 1057 (2011).
[3] L. Fu, Phys. Rev. Lett. **106**, 106802 (2011).
[4] R.-J. Slager, A. Mesaros, V. Juričić, and J. Zaanen, Nat. Phys. **9**, 98 (2013).
[5] R. S. K. Mong, A. M. Essin, and J. E. Moore, Phys. Rev. B **81**, 245209 (2010).
[6] A. M. Essin, J. E. Moore, and D. Vanderbilt, Phys. Rev. Lett. **102**, 146805 (2009).
[7] X.-L. Qi, T. L. Hughes, and S.-C. Zhang, Phys. Rev. B **78**, 195424 (2008).
[8] N. P. Armitage, E. J. Mele, and A. Vishwanath, Rev. Mod. Phys. **90**, 015001 (2018).
[9] N. R. Cooper, J. Dalibard, and I. B. Spielman, Rev. Mod. Phys. **91**, 015005 (2019).
[10] T. Ozawa, H. M. Price, A. Amo, N. Goldman, M. Hafezi, L. Lu, M. C. Rechtsman, D. Schuster, J. Simon, O. Zilberberg, and I. Carusotto, Rev. Mod. Phys. **91**, 015006 (2019).
[11] A. P. Schnyder, S. Ryu, A. Furusaki, and A. W. W. Ludwig, Phys. Rev. B **78**, 195125 (2008).
[12] J. Kruthoff, J. de Boer, J. van Wezel, C. L. Kane, and R.-J. Slager, Phys. Rev. X **7**, 041069 (2017).

[13] B. Bradlyn, L. Elcoro, J. Cano, M. G. Vergniory, Z. Wang, C. Felser, M. I. Aroyo, and B. A. Bernevig, Nature (London) **547**, 298 (2017).

[14] A. Bouhon and A. M. Black-Schaffer, Phys. Rev. B **95**, 241101(R) (2017).

[15] H. C. Po, A. Vishwanath, and H. Watanabe, Nat. Commun. **8**, 50 (2017).

[16] L. Fu and C. L. Kane, Phys. Rev. B **76**, 045302 (2007).

[17] H. Watanabe, H. C. Po, and A. Vishwanath, Sci. Adv. **4**, eaat8685 (2018).

[18] L. Elcoro, B. J. Wieder, Z. Song, Y. Xu, B. Bradlyn, and B. A. Bernevig, Nat. Commun. **12**, 5965 (2021).

[19] A. Bouhon, G. F. Lange, and R.-J. Slager, Phys. Rev. B **103**, 245127 (2021).

[20] T. Oka and H. Aoki, Phys. Rev. B **79**, 081406(R) (2009).

[21] T. Kitagawa, T. Oka, A. Brataas, L. Fu, and E. Demler, Phys. Rev. B **84**, 235108 (2011).

[22] H. Hübener, M. A. Sentef, U. De Giovannini, A. F. Kemper, and A. Rubio, Nat. Commun. **8**, 13940 (2017).

[23] T. Oka and S. Kitamura, Annu. Rev. Condens. Matter Phys. **10**, 387 (2019).

[24] M. S. Rudner and N. H. Lindner, Nat. Rev. Phys. **2**, 229 (2020).

[25] C. P. Weber, J. Appl. Phys. **129**, 070901 (2021).

[26] J. Struck, C. Ölschläger, M. Weinberg, P. Hauke, J. Simonet, A. Eckardt, M. Lewenstein, K. Sengstock, and P. Windpassinger, Phys. Rev. Lett. **108**, 225304 (2012).

[27] K. Jiménez-García, L. J. LeBlanc, R. A. Williams, M. C. Beeler, A. R. Perry, and I. B. Spielman, Phys. Rev. Lett. **108**, 225303 (2012).

[28] G. Jotzu, M. Messer, R. Desbuquois, M. Lebrat, T. Uehlinger, D. Greif, and T. Esslinger, Nature (London) **515**, 237 (2014).

[29] C. Weitenberg and J. Simonet, Nat. Phys. **17**, 1342 (2021).

[30] M. C. Rechtsman, J. M. Zeuner, Y. Plotnik, Y. Lumer, D. Podolsky, F. Dreisow, S. Nolte, M. Segev, and A. Szameit, Nature (London) **496**, 196 (2013).

[31] Y. H. Wang, H. Steinberg, P. Jarillo-Herrero, and N. Gedik, Science **342**, 453 (2013).

[32] J. W. McIver, B. Schulte, F.-U. Stein, T. Matsuyama, G. Jotzu, G. Meier, and A. Cavalleri, Nat. Phys. **16**, 38 (2020).

[33] M. Först, C. Manzoni, S. Kaiser, Y. Tomioka, Y. Tokura, R. Merlin, and A. Cavalleri, Nat. Phys. **7**, 854 (2011).

[34] E. J. Sie *et al.*, Nature (London) **565**, 61 (2019).

[35] A. S. Disa, M. Fechner, T. F. Nova, B. Liu, M. Först, D. Prabhakaran, P. G. Radaelli, and A. Cavalleri, Nat. Phys. **16**, 937 (2020).

[36] M. Y. Zhang, Z. X. Wang, Y. N. Li, L. Y. Shi, D. Wu, T. Lin, S. J. Zhang, Y. Q. Liu, Q. M. Liu, J. Wang, T. Dong, and N. L. Wang, Phys. Rev. X **9**, 021036 (2019).

[37] L. Luo, D. Cheng, B. Song, L.-L. Wang, C. Vaswani, P. M. Lozano, G. Gu, C. Huang, R. H. J. Kim, Z. Liu, J.-M. Park, Y. Yao, K. Ho, I. E. Perakis, Q. Li, and J. Wang, Nat. Mater. **20**, 329 (2021).

[38] N. Sirica *et al.*, Nat. Mater. **21**, 62 (2022).

[39] S. A. Sato, J. W. McIver, M. Nuske, P. Tang, G. Jotzu, B. Schulte, H. Hübener, U. De Giovannini, L. Mathey, M. A. Sentef, A. Cavalleri, and A. Rubio, Phys. Rev. B **99**, 214302 (2019).

[40] T. Nag, R.-J. Slager, T. Higuchi, and T. Oka, Phys. Rev. B **100**, 134301 (2019).

[41] M. N. Ali, Q. Gibson, S. Jeon, B. B. Zhou, A. Yazdani, and R. J. Cava, Inorg. Chem. **53**, 4062 (2014).

[42] T. Schumann, M. Goyal, H. Kim, and S. Stemmer, APL Mater. **4**, 126110 (2016).

[43] Z. Wang, H. Weng, Q. Wu, X. Dai, and Z. Fang, Phys. Rev. B **88**, 125427 (2013).

[44] See Supplemental Material at http://link.aps.org/supplemental/10.1103/PhysRevLett.128.066602 for details about the BCL setup, $\mathbf{k} \cdot \mathbf{p}$ model for Cd_3As_2, higher-order terms in the frequency expansion, temperature dependence of the gyrotropic magnetic effect, and technical details on surface-state calculations.

[45] M. Kargarian, M. Randeria, and Y.-M. Lu, Proc. Natl. Acad. Sci. U.S.A. **113**, 8648 (2016).

[46] T. Mikami, S. Kitamura, K. Yasuda, N. Tsuji, T. Oka, and H. Aoki, Phys. Rev. B **93**, 144307 (2016).

[47] S. Rahav, I. Gilary, and S. Fishman, Phys. Rev. A **68**, 013820 (2003).

[48] A. Eckardt and E. Anisimovas, New J. Phys. **17**, 093039 (2015).

[49] M. Bukov, L. D'Alessio, and A. Polkovnikov, Adv. Phys. **64**, 139 (2015).

[50] S. Jeon, B. B. Zhou, A. Gyenis, B. E. Feldman, I. Kimchi, A. C. Potter, Q. D. Gibson, R. J. Cava, A. Vishwanath, and A. Yazdani, Nat. Mater. **13**, 851 (2014).

[51] P. Villar Arribi, J.-X. Zhu, T. Schumann, S. Stemmer, A. A. Burkov, and O. Heinonen, Phys. Rev. B **102**, 155141 (2020).

[52] J. Ahn, S. Park, and B.-J. Yang, Phys. Rev. X **9**, 021013 (2019).

[53] F. N. Ünal, A. Bouhon, and R.-J. Slager, Phys. Rev. Lett. **125**, 053601 (2020).

[54] A. Bouhon, Q. Wu, R.-J. Slager, H. Weng, O. V. Yazyev, and T. Bzdušek, Nat. Phys. **16**, 1137 (2020).

[55] Q. Wu, A. A. Soluyanov, and T. Bzdušek, Science **365**, 1273 (2019).

[56] B. Jiang, A. Bouhon, Z.-K. Lin, X. Zhou, B. Hou, F. Li, R.-J. Slager, and J.-H. Jiang, Nat. Phys. **17**, 1239 (2021).

[57] S. Zhong, J. E. Moore, and I. Souza, Phys. Rev. Lett. **116**, 077201 (2016).

[58] J. Ma and D. A. Pesin, Phys. Rev. B **92**, 235205 (2015).

[59] R. Schönemann, G. Rodriguez, D. Rickel, F. Balakirev, R. D. McDonald, J. Evans, B. Maiorov, C. Paillard, L. Bellaiche, M. B. Salamon, K. Gofryk, and M. Jaime, arXiv:2103.08138.

[60] G. Resta, S.-T. Pi, X. Wan, and S. Y. Savrasov, Phys. Rev. B **97**, 085142 (2018).

[61] A. M. Turner, Y. Zhang, R. S. K. Mong, and A. Vishwanath, Phys. Rev. B **85**, 165120 (2012).

[62] C. Fang and L. Fu, Phys. Rev. B **91**, 161105(R) (2015).

[63] J. Ahn, S. Park, D. Kim, Y. Kim, and B.-J. Yang, Chin. Phys. B **28**, 117101 (2019).

[64] D. Vanderbilt, *Berry Phases in Electronic Structure Theory: Electric Polarization, Orbital Magnetization and Topological Insulators* (Cambridge University Press, Cambridge, England, 2018).